RSC Advances

PAPER

View Article Online
View Journal | View Issue

Cite this: *RSC Adv.*, 2025, **15**, 8443

Synthesis and DNA binding studies of novel triazine-isatin hybrids: experimental and computational insights†

Alia Mushtaq and Muhammad Moazzam Naseer *

DNA binding is a crucial determinant in developing novel anticancer agents, as it plays a key role in the mechanism of action for many chemotherapeutic drugs. In this study, a series of novel *s*-triazine-isatin hybrids (**7a–f**) was synthesized, and their binding interactions with salmon sperm DNA (SS-DNA) were investigated under physiological conditions (pH 7.4) using UV-vis absorption spectroscopy. The experimental findings demonstrated strong DNA-binding affinity through absorption and intensity shifts *via* groove-binding modes with SS-DNA. The binding constants (K_b) of synthesized hybrids with SS-DNA calculated from the Benesi–Hildebrand plot, ranged from 10^4 to 10^5 M^{-1}, with compound **7f** exhibiting the highest binding constant (9.51×10^5 M^{-1}) at 298 K, surpassing the reference cabozantinib. The Gibbs free energy change in the binding interaction of **7f**, was found to be $\Delta G = -34.1$ kJ mol^{-1} indicating a spontaneous binding process. The molecular docking results supported experimental findings with a docking score of −10.3 kcal mol^{-1} for **7f**, highlighting hydrophobic and hydrogen bonding interactions within the AT-rich region of DNA grooves. In addition, DFT and *in silico* studies provided insights into the charge density of structures and drug-likeness, hence the *s*-triazine-isatin hybrid core holds promise as a potential therapeutic agent.

Received 7th February 2025
Accepted 10th March 2025

DOI: 10.1039/d5ra00899a

rsc.li/rsc-advances

1. Introduction

Cancer continues to be a leading cause of morbidity and mortality worldwide, highlighting the critical need for ongoing research into novel therapeutic agents.[1,2] Despite significant progress in treatment options, challenges such as drug resistance and toxicity emphasize the urgent demand for new compounds that offer improved efficacy and selectivity.[3,4] Therefore, the design and development of small molecules with anticancer potential have attracted considerable attention due to their ability to target and modulate key biological pathways.[5–7]

DNA is a well-established target for anticancer drugs,[8] as interactions between drugs and DNA can disrupt cellular replication and transcription processes.[9–11] Small molecules interact with DNA through covalent or noncovalent mechanisms, modulating its structure and function.[12] Noncovalent interactions are typically classified into groove binding, intercalation, and electrostatic binding.[13] Intercalation involves the insertion of a small molecule between DNA base pairs, which distorts the DNA backbone.[14,15] In contrast, groove binding occurs within the minor or major grooves of DNA, facilitated by dispersion forces or hydrogen bonding, and is influenced by the structural and electronic properties of the small molecules.[14,15] Given the crucial role of DNA in essential cellular processes, studying its interactions with small molecules is vital for drug discovery, especially when designing novel therapeutic agents with enhanced specificity and efficacy.[16–21]

Triazines and isatin derivatives represent two pharmacophoric scaffolds that have demonstrated broad-spectrum biological activities, including anticancer properties.[22–26] Triazines, recognized for their versatility in medicinal chemistry, serve as the structural foundation for several commercially available anticancer drugs including altretamine, gedatolisib, and bimiralisib.[27–29] Similarly, isatin (indole-2,3-dione) and its derivatives have exhibited promising anticancer activities by targeting various cellular mechanisms, such as DNA interaction and enzyme inhibition.[30–32] Notably, isatin-based compounds are key components of FDA-approved anticancer drugs such as sunitinib and nintedanib.[33,34]

In recent years, pharmacophore hybridization has emerged as a promising strategy for developing novel anticancer agents, as different pharmacophores work synergistically to enhance biological activity.[35–39] In this context, both *s*-triazine and isatin have produced excellent results.[40,41] Given the importance of hybrid approach and our recent interest in developing anticancer agents based on *s*-triazine[42] and isatin,[43] herein we report the synthesis of a series of novel *s*-triazine-isatin hybrids (**7a–f**) and their evaluation for DNA binding properties using UV-vis

Department of Chemistry, Quaid-i-Azam University, Islamabad 45320, Pakistan. E-mail: moazzam@qau.edu.pk

† Electronic supplementary information (ESI) available. See DOI: https://doi.org/10.1039/d5ra00899a

absorption spectroscopy. Salmon sperm DNA (SS-DNA) is typically favored as a DNA model for its availability and cost-effectiveness,[10] was employed in this study to investigate its interaction with newly synthesized compounds, providing insights into their binding mechanisms and therapeutic potential. In addition, molecular docking, density functional theory (DFT) analyses, and *in silico* ADMET profiling were performed to predict binding modes, binding strength, specificity, and drug-likeness. The integration of experimental and computational findings highlights the remarkable potential of these novel hybrids as promising anticancer agents.

2. Results and discussion

2.1 Chemistry

A convergent synthetic pathway was utilized for the synthesis of *s*-triazine-isatin hybrids (**7a–f**) (Scheme 1). Fragment I, diphenoxy-linked hydrazinyl *s*-triazines (**3**) were synthesized by reacting trichlorotriazine (**1**) with 2 equivalents of various substituted phenols using anhydrous potassium carbonate as an acid scavenger for liberated hydrochloric acid.[44] Maintaining reaction conditions was also crucial, as the reaction was initiated at ice-cold temperatures and subsequently transitioned to room temperature to minimize the formation of tri-substituted side products. The diphenoxy-linked *s*-triazines (**2**) were subsequently reacted with hydrazine monohydrate at room temperature,[45] yielding fragment I (**3**). Likewise, the alkylation reaction of isatin (**4**) with 2-chloro-*N*-(4-bromophenyl)acetamide (**5**) in the presence of DMF, yielded fragment II, 4-bromophenyl acetamide pendant isatin (**6**), in good yield.[46,47] Finally, the two synthesized fragments were refluxed in the presence of ethanol and a few drops of glacial acetic acid to afford series of phenoxy-linked *s*-triazine-based hydrazones of *N*-alkylated isatins (**7a–f**).

The chemical structures of the newly synthesized compounds (**7a–f**) were elucidated through comprehensive characterization using spectroscopic techniques, including FTIR, NMR, and MS analyses.

In the ^{1}H NMR spectrum of compound **7a**, the hallmark singlets for –NH protons of hydrazone moiety and amide linkage appeared at 12.65 ppm and 10.51 ppm respectively. Moreover, the absence of $-NH_2$ protons of compound **6** also evidenced the hydrazone formation by the condensation of hydrazinyl *s*-triazine scaffold with the carbonyl of isatin. The aromatic region is characterized by multiplets corresponding to an 18-proton integration within the δ 7.16–7.58 range, validating the substitution pattern on the aromatic rings. The singlet at 4.66 ppm integrating two protons was assigned to methylene group of *N*-phenylacetamide ($-N-CH_2$). Furthermore, in the ^{13}C NMR spectra of compound **7a**, the most deshielded signals at 167.5 ppm and 165.5 ppm were accredited to the carbonyl of amide moieties. The absence of keto-carbonyl carbon further supported the formation of hydrazones. The signal in the aliphatic region at 43.2 suggested the presence of methylene group of *N*-phenylacetamide ($-NCH_2$) moeity. Moreover, the signals observed in the range of 110.8 to 161.7 were attributed to the aromatic carbons of the *s*-triazine-isatin hybrids (see ESI† for further details).

The mass spectra of the *s*-triazine-isatin hybrids (**7a–f**) also revealed parent ion peaks [M − 1], consistent with their respective molecular formulas. Furthermore, the FTIR spectral analysis revealed distinct absorption bands characteristic of the functional groups, supporting the structural frameworks of the synthesized compounds (**7a–f**).

2.2 DNA binding studies

In pharmacology, assessing the DNA-binding affinity of newly synthesized compounds is a key approach for evaluating their antitumor potential.[42,48] Investigating these drug–DNA interactions is critical to understanding their biological mechanisms and optimizing their efficacy.[49–51]

UV-visible spectroscopy is a powerful tool for investigating the binding modes and strengths of DNA–compound interactions.[52,53] The absorption spectra for compounds (**7a–f**) were recorded at a constant concentration of 50 μM, with varying the concentration of SS-DNA (5–35 μM).[10] As expected, all unbound derivatives (**7a–f**) displayed absorption within the 300–450 nm range, with absorption maxima falls in the range of 340–351 nm. The findings revealed that successive additions of DNA

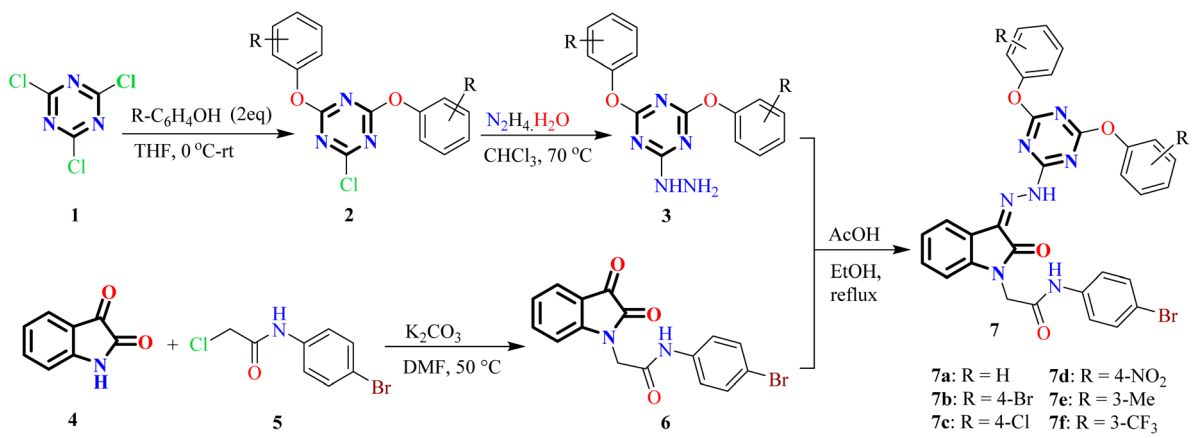

Scheme 1 Synthetic pathway of various *s*-triazine-isatin hybrids (**7a–f**).

induced characteristic spectral changes, including hyperchromic and hypochromic effects, accompanied by bathochromic (red) or hypsochromic (blue) shifts in the UV-vis spectral bands. These spectral shifts are indicative of robust interactions between the synthesized compounds (**7a–f**) and the SS-DNA double helix[54] (Fig. 1).

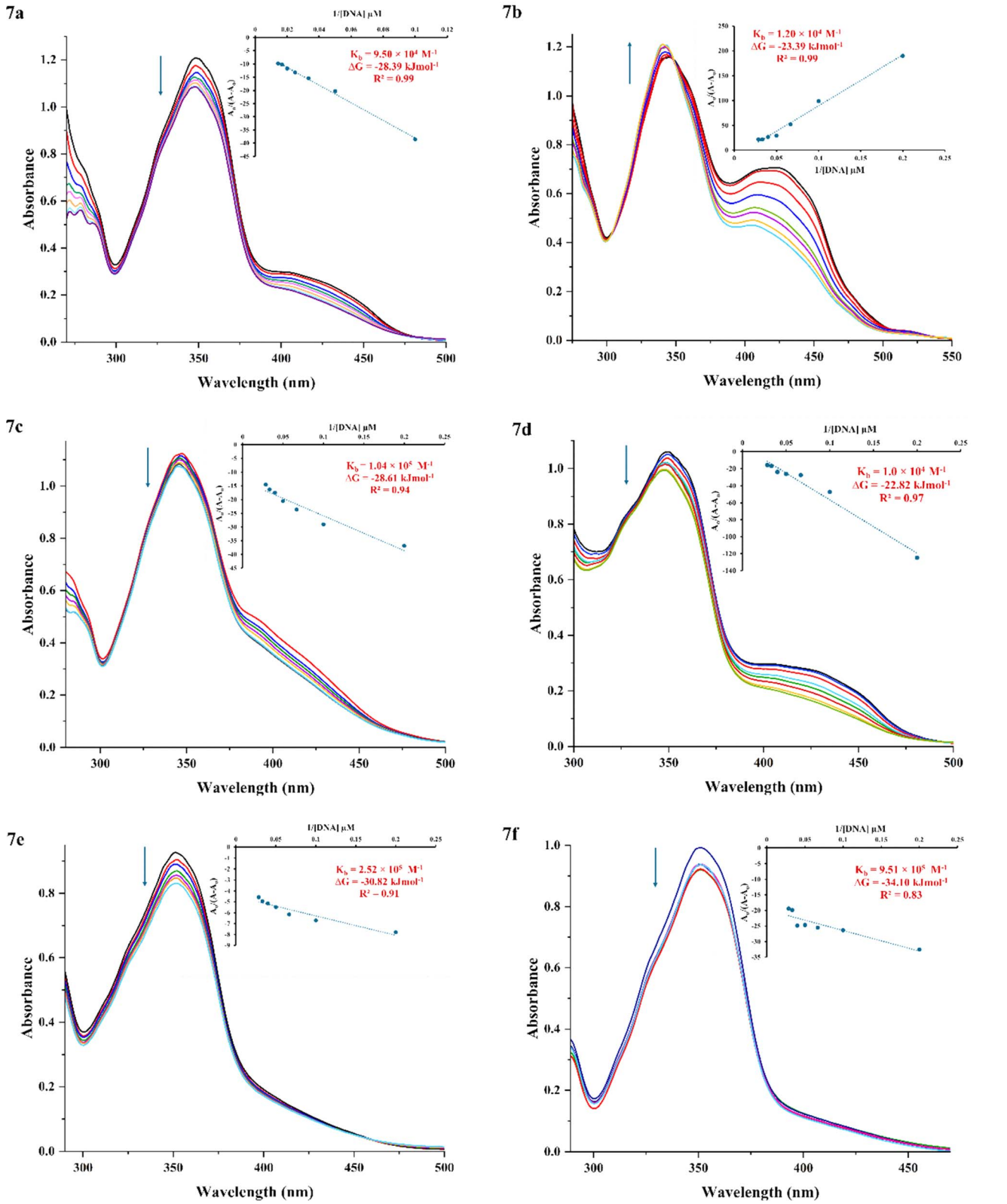

Fig. 1 UV-vis absorption spectra of compounds (**7a–f**) at pH 7.4 and room temperature, with and without varying SS-DNA concentrations (5–35 μM), demonstrating spectral shifts indicative of groove binding interactions. Inset: plot of $A_0/(A - A_0)$ as a function of 1/[DNA].

Table 1 Results of the determination of the binding constants (K_b) at room temperature and binding free energies (ΔG) of compounds (**7a–f**)–DNA complex

Compounds	R	K_b (M^{-1})	ΔG (kJ mol^{-1})
7a	H	9.50×10^4	−28.39
7b	4-Br	1.20×10^4	−23.39
7c	4-Cl	1.04×10^5	−28.61
7d	4-NO_2	1.0×10^4	−22.82
7e	3-Me	2.52×10^5	−30.82
7f	3-CF_3	9.51×10^5	−34.10
Cabozantinib	_	5.79×10^5 (ref. 10)	−32.87 (ref. 10)

Among the synthesized compounds, **7b** (R = 4-Br) uniquely displayed a hyperchromic effect and a pronounced red shift (6 nm) in the UV-vis spectra, signifying notable conformational and structural changes in DNA upon interaction due to π–π* and *n*–π* transitions.[55,56] However, the remaining compounds showed a hypochromic shift, with slight blue shift or without significant red shift (Fig. 1) indicating aromatic electron stabilization and enhanced compound-DNA complex stability *via* major or minor groove binding mode.[8,57,58]

Binding affinity, a fundamental determinant of drug potency, is quantified using the association constant (K_b), where higher K_b values reflect stronger and more effective binding interactions.[14,59] The binding constants (K_b) for compound-DNA complexes were calculated using the Benesi–Hildebrand equation, to assess the binding strength of the synthesized derivatives (**7a–f**). These values were determined from the $A_0/(A - A_0)$ intercept-to-slope ratios plotted against 1/[DNA].[60] At room temperature, the K_b values were found to range from 10^4 to 10^5, with higher values signifying a greater affinity for DNA binding. The K_b values for the compounds (**7a–f**) followed the ascending order: **7d** < **7b** < **7a** < **7c** < **7e** < **7f** (Table 1). These variations in the binding strength were attributed to the differing electronic contributions of the substituents, influencing the interaction of the compounds with SS-DNA.

Notably, compound **7f** (R = 3-CF_3) exhibited the highest binding constant ($K_b = 9.51 \times 10^5$ M^{-1}), highlighting its superior interaction profile compared to other derivatives. This aligns with its significant hypochromic effect without significant red shift, suggesting its strong binding affinity and potential to bind in the grooves of DNA, consistent with the literature.[14,61,62] Although, its binding constant was lower than that of the classical intercalators like ethidium bromide (1.4×10^6 M^{-1}),[63] it aligned with the typical range for DNA groove binders like cabozantinib (Table 1).[10,64–67] These results underscore the influence of substituents on DNA binding efficacy, particularly the role of electronic and hydrophobic effects in enhancing groove binding.

Additionally, the variation in light absorption observed across all compounds, does not correlate with DNA binding strength. Although the derivative **7b**, exhibited the greatest hyperchromic and bathochromic shifts, it did not have the highest K_b value, likely due to electronic and lipophilic effects.[58] Substituents at the para position with smaller electronic profiles (σ) were found to positively influence DNA interactions. However, the substituents with positive lipophilicity (+π) *i.e.* CF_3, as indicated in Craig Diagram,[68] demonstrated higher K_b values (Table 1). Besides that, the strong electron-withdrawing nature of the CF_3 group reduces the availability of free electron pairs, facilitating hydrophobic interactions and stabilizing the DNA-compound complex.[58] In comparison, derivatives with smaller or less lipophilic substituents, such as **7d** (4-NO_2), exhibited lower binding constants (1.0×10^4 M^{-1}), consistent with reduced hydrophobic stabilization. These findings emphasize the pivotal role of substituents in modulating electronic properties and lipophilicity, directly impacting binding strength and selectivity.

The Van't Hoff equation ($\Delta G = -RT \ln K_b$) was used to determine the Gibbs free energy (ΔG) for the interaction between the tested compounds (**7a–f**) and SS-DNA.[10] The compound **7f** (R = 3-CF_3) exhibited the most negative ΔG value of −34.1 kJ mol^{-1} (Table 1), surpassing the standard cabozantinib,[10] indicating a spontaneous and thermodynamically favorable binding process under the given conditions.[42] Henceforth, these findings suggested that compounds (**7a–f**) hold potential as future therapeutic agents for treating various diseases.

2.3 Molecular docking

The rational design of effective anticancer agents involves considering a drug's ability to bind to DNA because this binding makes it possible to identify particular DNA regions that are targeted through non-covalent interactions.[10,69] When combined with experimental methods, molecular docking studies provide useful information for identifying possible drug candidates.[70] Docking analyses were performed using AutoDockTools 1.5.7 to assess the interaction mode and binding

Table 2 Estimated docking scores and interaction profiles of compounds (**7a–f**) with DNA (3EY0)[a]

Compds	R	Binding energy (kcal mol^{-1})	Compound-DNA interactions	
			Hydrogen bonding	Hydrophobic
7a	H	−8.7	dt4 (A), da5 (A), da 7 (B)	dt2 (A), da3 (A), dt4 (B), da5 (B), dt6 (B)
7b	4-Br	−8.7	da5 (A)	dt2 (A), da3 (A), dt4 (A), dt4 (B), da5 (B), dt6 (B), da7 (B)
7c	4-Cl	−8.9	da 7 (B)	dt2 (A), da3 (A), dt4 (A), dt4 (B), da5 (B), dt6 (B)
7d	4-NO_2	−8.5	—	dt4 (A), da5 (A), dt6 (A), dt6 (B), da7 (A), da7 (B), dt8 (B), da9 (B)
7e	3-Me	−8.9	da5 (A), da7 (B)	dt2 (A), da3 (A), dt4 (A), dt4 (B), da5 (B), dt6 (B)
7f	3-CF_3	−10.3	da7 (B)	da5 (A), da5 (B), dt6 (A), dt6 (B), da7 (A), dt8 (A), dt8 (B), da9 (B)

[a] da: deoxy-adenine, dt: deoxy-thymine.

affinity of synthesized *s*-triazine-isatin hybrids (**7a–f**) with DNA (PDB ID: 3EY0).[71] The results revealed significant binding affinity of all studied compounds with the double-helix DNA (sequence: 5′-(ATATATATAT)-3′), with docking scores ranging from −8.5 to −10.3 kcal mol^{-1} (Table 2). Notably, the 3-trifluoromethyl-substituted derivative **7f** showed the highest binding affinity, scoring −10.3 kcal mol^{-1}.

The representative docking poses of compounds (**7a–f**) revealed their interaction with DNA through a mixed binding mode in both the major and minor grooves (Fig. 2). Molecular docking results supported the experimental DNA binding studies, showing hydrogen bonding and hydrophobic interactions between the compounds and DNA (3EY0). Compounds **7a**, **7b**, **7c** and **7e** incorporating R=H, 4-Br, 4-Cl, and 3-Me

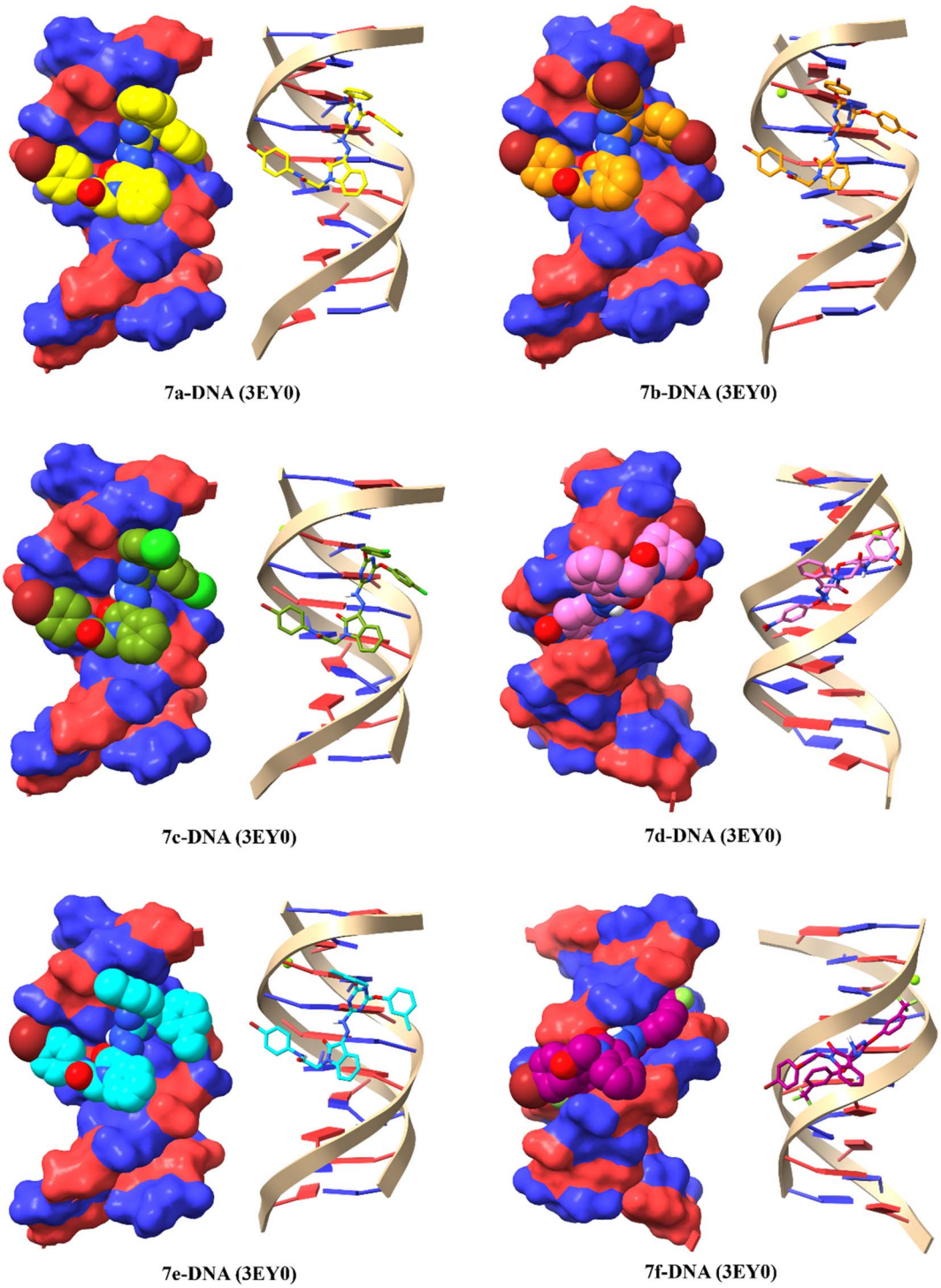

Fig. 2 3D docked view of compounds (**7a–f**) with the nitrogenous base pairs of DNA (3EY0): and cartoon presentation (right) and surface view (left); deoxy adenine-da (red), deoxy thymine-dt (blue), **7a** (yellow), **7b** (orange), **7c** (green), **7d** (pink), **7e** (cyan) **7f** (purple).

respectively, displayed binding interactions in the major groove of DNA. However, compounds **7d** (R = 4-NO_2) and **7f** (R = 3-CF_3) were found to bind in the minor groove of DNA (Fig. 2). The docking protocol was also validated by superimposing the co-crystallized ligand on the redocked structure, which exhibited the RMSD value of 1.4292 Å (Fig. S1†).

The hydrogen bonding and hydrophobic interactions of compounds (**7a–f**) are presented in Fig. 3. The top scorer compound **7f** displayed two hydrogen bond interactions (2.91 and 3.30 Å distance) with the da7 base of chain B (Table 2), which corroborated the hydrogen bond interactions of the standard tyrosine kinase inhibitor, cabozantinib (2.64 and 3.08 Å distance).[10] In addition, hydrophobic interactions with the same nitrogenous pairs dt8, dt6, da5, da7, and da9 were found, suggesting similar sorts of interactions in the binding site of DNA as in the case of standard cabozantinib. Furthermore, the NH group of hydrazones, lactum carbonyl of isatin and oxygen of phenoxy groups in compounds (**7a–f**) were mainly involved in the hydrogen bonding interactions with adenine and thymine base pairs of DNA (Fig. 3) The hydrazone functionality is also well-recognized for its antitumor properties.[72]

2.4 DFT studies

Density functional theory (DFT) offers a framework for understanding chemical reactivity through the electron density of a system.[72,73] The parameters obtained from the optimized geometries (Fig. 4) of the synthesized hybrids (**7a–f**) provide valuable insights into molecular interactions, complementing the findings from molecular docking analyses.[43,74]

FMO analysis of *s*-triazine-isatin hybrids (**7a–f**), revealed variations in electronic properties influenced by substituents.[8] Global reactivity descriptors including E_{HOMO}, E_{LUMO}, energy gap (ΔE_{gap}), electron affinity (E_A), ionization potential (I_P), electronegativity (χ), chemical potential (μ), chemical hardness (η), chemical softness (S), and electrophilicity (ω) (Table 3) were determined using B3LYP method and 3-21G basis set.[75] All the synthesized compounds (**7a–f**) displayed dipole moments within the suitable range of 3.18 to 5.48 debye (Table 1), indicative of significant charge separation that enhances solubility in polar solvents such as water and highlights suitable polarity for drug-like behavior.[76] The most potent compound **7f** (R = 3-CF_3), exhibited dipole moments of 5.48 D, which fall well within the optimal range for drug-like molecules, suggesting an

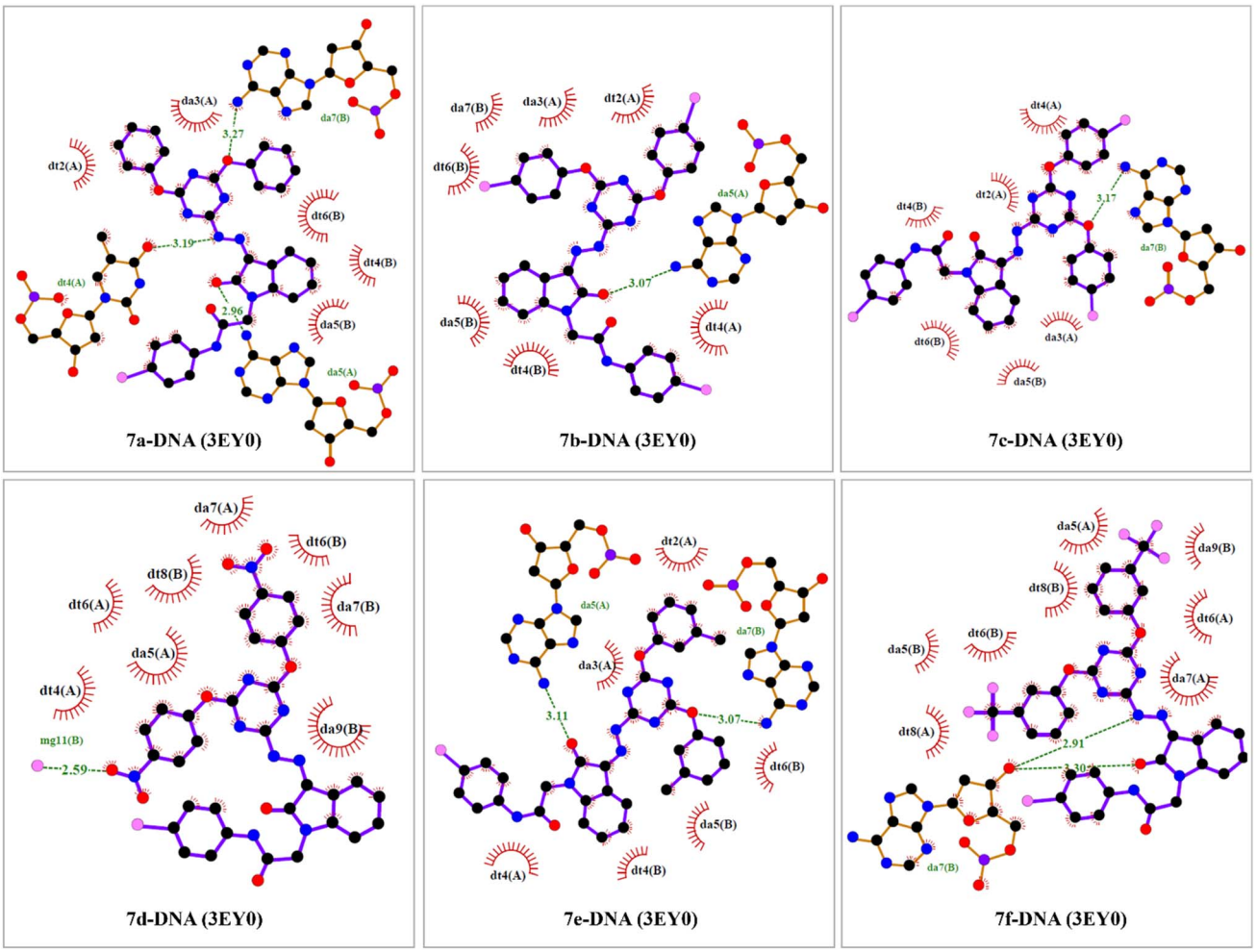

Fig. 3 2D schematic representation of the binding interactions in compounds (**7a–f**)–DNA complexes, illustrating hydrogen bond interactions (green dashed lines), hydrogen bond lengths (Å), and hydrophobic interactions (red rays).

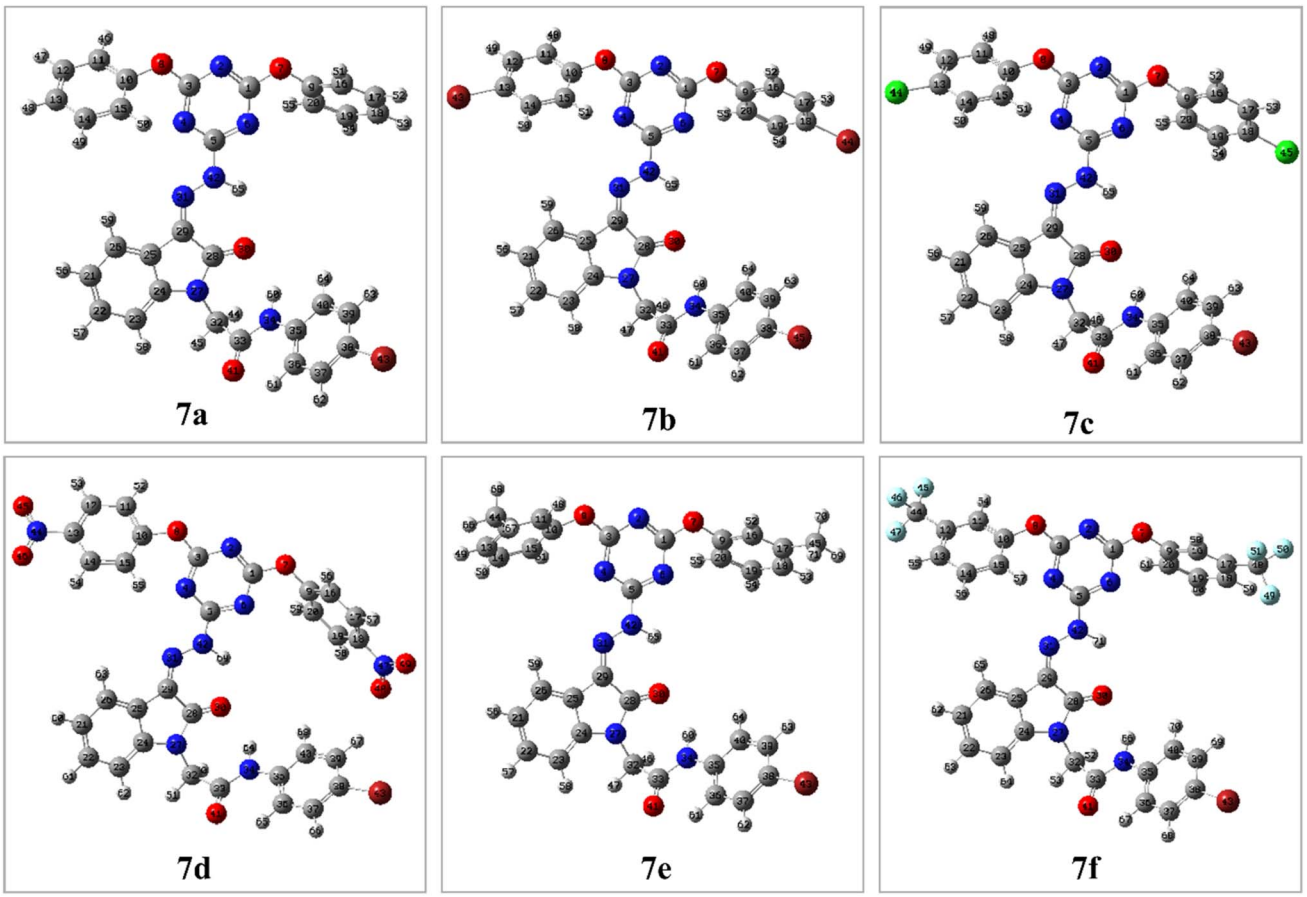

Fig. 4 Optimized structures of *s*-triazine-isatin hybrids (**7a–f**).

ideal balance of charge separation to ensure enhanced solubility while maintaining favorable pharmacokinetic properties.

In addition, E_{HOMO} reflects the greater electron-donating ability of a compound, whereas higher E_{LUMO} represents its electron-withdrawing capacity.[77] The negative energies of E_{HOMO} and E_{LUMO} indicated the inherent stability of all the studied compounds (**7a–f**) (Table 3). The energy gap ($\Delta E_{LUMO-HOMO}$) reflects the chemical behavior and kinetic stability of compounds. The E_{HOMO} and E_{LUMO} values (−5.94 to −5.79 eV and −2.94 to −2.55 eV, respectively) and energy gaps (ΔE_{gap}, 2.85–3.28 eV) suggested inherent stability and reactivity (Table 3). Compounds **7d** (R = 4-NO_2) and **7f** (R = 3-CF_3), incorporating electron-withdrawing groups, displayed the lower ($\Delta E_{LUMO-HOMO}$) values, indicating their high propensity for chemical reactivity due to smaller gaps. This characteristic makes these compounds promising candidates for drug development due to their efficient electron-donating and electron-accepting capabilities.

Ionization potential (I_P) and electron affinity (E_A) correlated with these orbital energies, while electronegativity (χ) values for compounds (**7a–f**) ranged from 4.19 eV (**7e**; R = 3-Me), to 4.39 eV (**7f**; R = 3-CF_3) (Table 3), reflecting a strong electron-attracting tendency due to the electronic effects of the substituents. Furthermore, these reactivity indices quantify the tendency of chemical species to interact with electrons. A strong nucleophile is characterized by low values of chemical potential (μ) and electrophilicity (ω), while a strong electrophile exhibits high values of these parameters.[78] The hardness and softness values classify these compounds as relatively soft, implying higher reactivity. Likewise, the electrophilicity index (ω) varied from 0.71 eV to 0.82 eV (Table 3) with higher values denoting an increased ability to accept electrons. Compound **7d** exhibited the lowest hardness (η = 1.425 eV), highest softness (S = 0.351 eV), and lowest electrophilicity index (ω = 0.71 eV), signifying high reactivity and nucleophilic tendency. In contrast, **7e** had the highest hardness (η = 1.64 eV) and electrophilicity (ω = 0.82 eV), indicating greater stability and electron-accepting potential (Table 3). These results highlight the impact of substituents on the stability and reactivity of *s*-triazine-isatin hybrids (**7a–f**), emphasizing their potential as adaptable candidates for drug development.

Fig. 5 illustrates that the HOMO orbitals of compounds (**7a–f**) are primarily localized on the *N*-phenylacetamide motif, while the LUMO orbitals are distributed across the π-systems of the *s*-triazine moiety and isatin scaffold. The spatial distribution highlights key regions for potential biological interactions, as illustrated in Fig. 5, which depicts the distinct electron-dense regions within the hybrids.

The DFT results also complement the molecular docking findings, providing a holistic understanding of the electronic

Table 3 DFT analysis parameters of the newly synthesized *s*-triazine-isatin hybrids (**7a–f**)

Compds	R	Dipole moment (Debye)	E_{HOMO} (eV)	E_{LUMO} (eV)	Energy gap (ΔE_{Gap})	Ionization potential IP (eV)	Electron affinity E_A (eV)	Electro-negativity χ (eV)	Electro-chemical potential μ (eV)	Hardness η (eV)	Softness S (eV)	Electro-philicity ω (eV)
7a	H	3.96	−5.85	−2.60	3.25	5.85	2.60	4.23	1.625	1.625	0.308	0.81
7b	4-Br	3.77	−5.88	−2.71	3.17	5.88	2.71	4.30	1.585	1.585	0.315	0.79
7c	4-Cl	3.67	−5.89	−2.73	3.16	5.89	2.73	4.31	1.58	1.58	0.316	0.79
7d	4-NO_2	3.70	−5.79	−2.94	2.85	5.79	2.94	4.37	1.425	1.425	0.351	0.71
7e	3-Me	3.18	−5.83	−2.55	3.28	5.83	2.55	4.19	1.64	1.64	0.305	0.82
7f	3-CF_3	5.48	−5.94	−2.84	3.10	5.94	2.84	4.39	1.55	1.55	0.322	0.78

and structural features that contribute to the bioactivity of compounds (**7a–f**). Compounds with enhanced electron transfer capabilities may more readily bind to macromolecules such as DNA or proteins due to their improved compatibility with macromolecular structures.[79] The charge transfer interactions revealed by the HOMO–LUMO transitions align with docking predictions of binding affinity, highlighting the potential of synthesized *s*-triazine-isatin hybrids (**7a–f**) for stable interactions with biological targets. Moreover, MEP analysis[80] (Fig. 5) provided critical insights into the electron distribution, identifying electron-rich (red) and electron-poor (blue) regions that corroborate docking-derived binding sites.[81] Notably, the electron-deficient *s*-triazine ring and nucleophilic oxygen atoms, highlighted in MEP, correspond precisely to the key interaction sites predicted by docking simulations. This convergence between DFT and docking results not only underscores the reactivity profiles of compounds (**7a–f**) but also strengthens their potential as targeted anticancer agents.

2.5 *In silico* pharmacokinetic profiling

Pharmacokinetic evaluation is a cornerstone in drug discovery, offering critical insights into the bioavailability, absorption, distribution, and overall drug-like properties of candidate molecules.[82] The *in silico* pharmacokinetic parameters of the synthesized compounds (**7a–f**) were assessed using SwissADME[83] and pkCSM tools,[84] with the results summarized in Table 4.

The compounds (**7a–f**) exhibited favorable physicochemical and pharmacokinetic properties, aligning with Lipinski's rule of five,[87] which indicated their potential for favorable oral bioavailability.[88] Parameters such as the log of the octanol–water partition coefficient (log *P*), log aqueous solubility (log *S*), and Topological Polar Surface Area (TPSA) fell within acceptable ranges for oral drug candidates.[58,89] Particularly, the LogP values, representing lipophilicity, were found within a range (3.44–6.77) consistent with drug-likeness, with most compounds demonstrating higher lipophilicity compared to cabozantinib (4.40), supporting adequate membrane permeability. However, more negative aqueous solubility (Log *S*) values for compounds **7b**, **7c**, and **7f** (−9.73, −9.09, and −9.65, respectively) than for cabozantinib (−7.22), suggested reduced solubility. Conversely, compounds **7a** and **7d** showed relatively better solubility profiles, closer to the standard (Table 4).

The topological polar surface area (TPSA), associated with drug absorption and blood–brain barrier penetration, was 130.93 Å^2 for most compounds, remained below the threshold of 140 Å^2 (Table 4) ensuring efficient transmembrane diffusion. Except compound **7d**, which exhibited a higher TPSA of 222.57 Å^2 suggesting reduced permeability potential compared to the other derivatives and cabozantinib (98.78 Å^2). Likewise, most compounds displayed higher Caco-2 permeability than cabozantinib (0.166), while compound **7d** showed a negative value (−0.36), further confirming its limited permeability.

The intestinal absorption percentages, predicted through pkCSM, demonstrated excellent absorption potential for all synthesized compounds (**7a–f**), indicating effective absorption

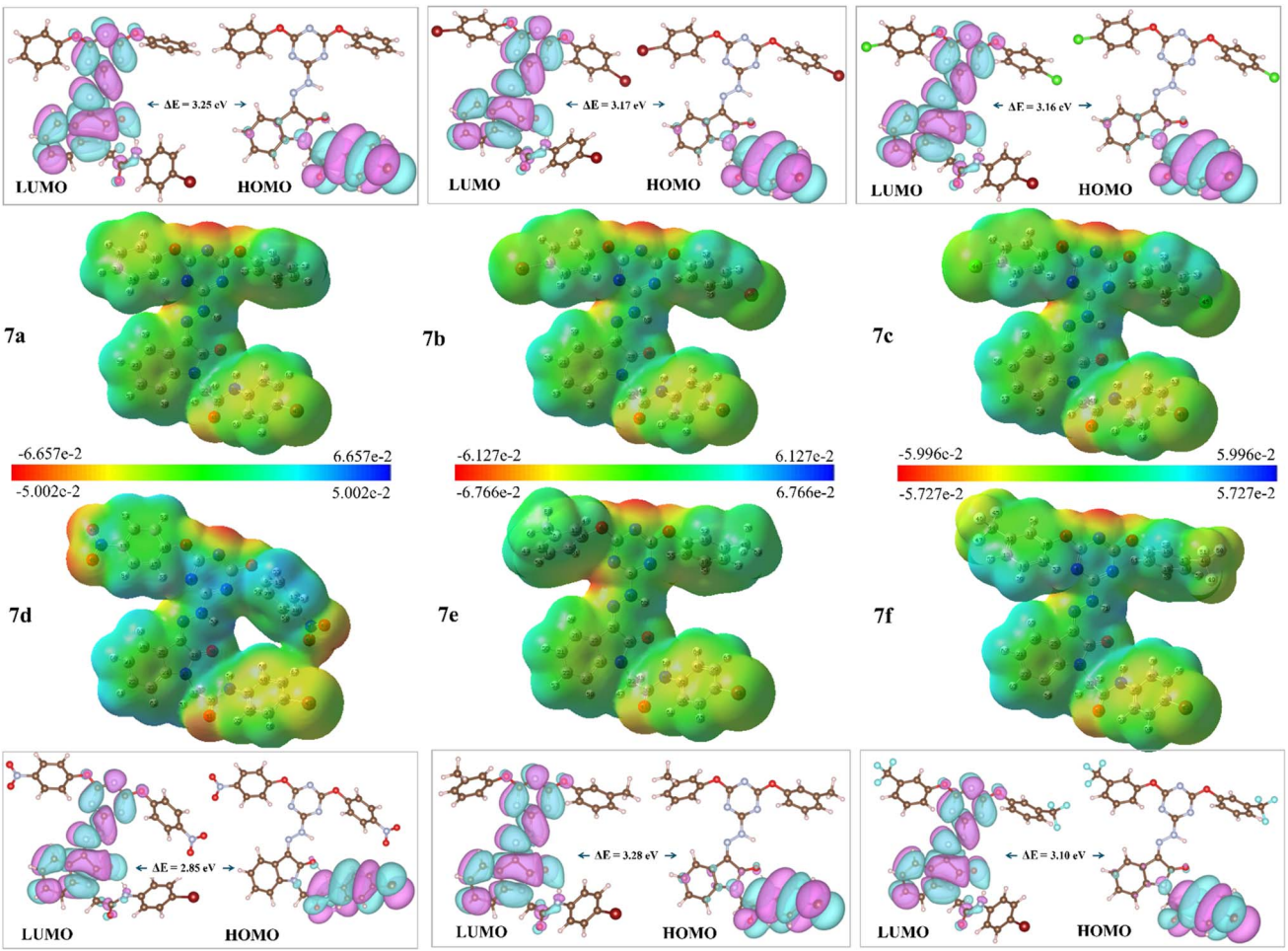

Fig. 5 HOMO, LUMO and MESP diagram of *s*-triazine-isatin hybrids (**7a–f**).

with values exceeding 98% for human intestinal absorption.[90] The steady-state volume of distribution (VDss) values suggested intermediate tissue distribution for most compounds, reflecting a balanced partitioning between plasma and tissues. Compounds (**7a–f**) had better tissue distribution than cabozantinib (−1.023), with the highest VDss observed for **7f** (−0.238), implying better systemic distribution. Exceptions with lower VDss values could be attributed to specific structural features influencing solubility and ionization capacity, such as in compound **7d** with its higher TPSA.

Overall, the pharmacokinetic profiles of synthesized compounds (**7a–f**) suggest that these hybrids are well-suited for further investigations, with promising absorption, distribution, and bioavailability characteristics. These findings highlight their potential as orally active anticancer agents, warranting advanced preclinical evaluations.

Table 4 *In silico* pharmacokinetic parameters of compounds (**7a–f**) estimated through SwissADME and pkCSM web servers

Compounds	Log P^a	Log S^b	TPSA^c (Å^2)	Caco-2 perm^d	Int. abs^e	VDss^f
7a	4.85	−7.90	130.93	0.616	100	−0.437
7b	6.11	−9.73	130.93	0.425	100	−0.342
7c	6.01	−9.09	130.93	0.42	100	−0.367
7d	3.44	−8.05	222.57	−0.36	98.11	−1.103
7e	5.40	−8.51	130.93	0.441	100	−0.311
7f	6.77	−9.65	130.93	0.426	100	−0.238
Cabozantinib	4.40	−7.22	98.78	0.166	100	−1.023

[a] Log of octanol–water partition coefficient (SwissADME[83]). [b] Log of aqueous solubility (SwissADME[83]). [c] Topological Polar Surface Area (TPSA) (SwissADME[83]). [d] Caco-2 cell permeability as estimation of absorption at human intestinal mucosa[85] (pkCSM prediction[86]). [e] Proportion (%) of compound absorbed through the human small intestine[85] (pkCSM prediction[86]). [f] Steady-state volume of distribution (VDss) (pkCSM prediction[86]).

3. Conclusions

The synthesis and characterization of novel *s*-triazine-isatin hybrids (**7a–f**) demonstrated their structural integrity and potential for biological applications, by revealing their strong potential as DNA-binding agents. Spectroscopic analyses and molecular docking studies revealed strong SS-DNA binding, particularly for the 3-CF_3 substituted compound **7f**, which exhibited the highest binding constant, favorable thermodynamics and the highest docking score. DFT calculations and *in silico* pharmacokinetic results further supported their suitability as drug candidates, highlighting optimal electronic properties and polarity for pharmacological activity. Overall, this study underscores the therapeutic potential of *s*-triazine-isatin hybrids as DNA-binding agents. The integration of spectroscopic analyses and computational results provides a comprehensive understanding of their interaction profiles. These findings establish a robust foundation for future studies, including *in vitro* and *in vivo* evaluations, to explore the clinical applicability of these hybrids as anticancer agents. Furthermore, the insights gained on substituent effects can guide the rational design of next-generation DNA-targeted therapeutics.

4. Experimental

4.1 Computational

The Gaussian 09 software package was used to optimize the molecular structures of all synthesized compounds.[91] To determine the electronic properties of the synthesized compounds, the optimized structures were employed. HOMO, LUMO and other descriptors were computed using GaussView6. AutodockVina 1.5.7 (ref. 71) was used to conduct the molecular docking studies, while for visualization the Discovery Studio,[92] PyMOL,[93] LigPlot + V1.4.5,[94] ChimeraX 1.4,[95] and VESTA 3.5.8 (ref. 96) were utilized. The reported grid point sizes (80, 60, 60) and coordinates (16.394, 10.415, 90.220) were employed for docking analyses.[10]

4.2 UV-visible spectroscopic analysis of DNA binding interactions

The SS-DNA (Sigma-Aldrich) stock solution was prepared in distilled water and kept on stirring for 24 h. DNA's purity from protein contamination was confirmed by A_{260}/A_{280} ratio of 1.89. The solution was further diluted 10-fold to obtain maximum absorbance at 260 nm. Using a molar absorptivity coefficient (ε) of 6600 M^{-1} cm^{-1} at 260 nm, the concentration of DNA was determined.[52] Shimadzu 1700 UV-visible spectrophotometer was utilized to acquire UV-vis absorption spectra. After preparing compound solutions (50 μM) in DMSO, their spectra were recorded without DNA, followed by measurements at varying DNA concentrations (5–35 μM).[42]

4.3 Synthetic procedure for the synthesis of *s*-triazine-isatin hybrids (7a–f)

To a solution of 4-bromophenyl acetamide pendant isatin **6** (0.25 mmol, 1.0 eq.) in ethanol, glacial acetic acid (few drops) was added followed by the addition of phenoxy-linked hydrazinyl *s*-triazines (**3**) (0.25 mmol, 1.0 eq.) The reaction progress was monitored at regular intervals using thin-layer chromatography. Hydrazones (**7a–f**) were precipitated out from the reaction mixture after 3–4 hours of reflux, which were subsequently filtered, dried, and recrystallized from ethanol to yield the pure product.

4.3.1 (*Z*)-*N*-(4-Bromophenyl)-2-(3-(2-(4,6-diphenoxy-1,3,5-triazin-2-yl)hydrazineylidene)-2-oxoindolin-1-yl)acetamide (7a). Yellow solid; melting point: 236–237 °C; R_f: 0.59 ($CHCl_3$, MeOH, 9 : 1); yield: 85%; FT-IR $\bar{\nu}$ (cm^{-1}): 1209 (C–N stretch; lactam), 1281 (C_{sp^2}–O stretch; ether), 1467 (C_{sp^3}–H bend; methylene), 1470, 1541 (C=C stretch; aromatic), 1619 (C=N stretch; imine), 1686, 1737 (C=O stretch; amide), 2971, (C_{sp^3}–H stretch), 3049, 3129 (C_{sp^2}–H stretch), 3225, 3300 (N–H stretch); ^{1}H NMR (300 MHz, DMSO-d_6) δ (ppm): 12.65 (s, 1H, –NH), 10.51 (s, 1H, –NH), 7.58–7.16 (m, 18H, Ar–H), 4.66 (s, 2H, $-CH_2$), 4.71 (t, 2H, ^3J = 6 Hz, $-OCH_2$), 4.14 (t, 2H, ^3J = 6 Hz, $-CH_2$ triazole); ^{13}C NMR (75 MHz, DMSO-d_6) δ (ppm): 167.2, 165.3, 161.7, 152.1, 143.4, 138.2, 135.5, 132.1, 131.9, 129.9, 126.3, 123.8, 122.0, 121.7, 119.4, 115.8, 110.8, 43.2; UV-vis (DMSO, nm) 348 (π–π*); LC-MS *m/z* 636.0 [M − 1]

4.3.2 (*Z*)-2-(3-(2-(4,6-Bis(4-bromophenoxy)-1,3,5-triazin-2-yl)hydrazineylidene)-2-oxoindolin-1-yl)-*N*-(4-bromophenyl)acetamide (7b). Yellow solid; melting point: 251–253 °C; R_f: 0.55 ($CHCl_3$, MeOH, 9 : 1); yield: 85%; FT-IR $\bar{\nu}$ (cm^{-1}): 1210 (C–N stretch; lactam), 1348 (C_{sp^2}–O stretch; ether), 1477 (C_{sp^3}–H bend; methylene), 1481, 1546 (C=C stretch; aromatic), 1619 (C=N stretch; imine), 1654, 1738 (C=O stretch; amide), 2836, 2935 (C_{sp^3}–H stretch), 3064, 3124 (C_{sp^2}–H stretch), 3253, 3300 (N–H stretch); ^{1}H NMR (300 MHz, DMSO-d_6) δ (ppm): 12.71 (s, 1H, –NH), 10.52 (s, 1H, –NH), 8.01–6.70 (m, 16H, Ar–H), 4.67 (s, 2H, $-CH_2$); ^{13}C NMR (75 MHz, DMSO-d_6) δ (ppm): 172.1, 165.8, 163.9, 151.2, 151.1, 144.8, 143.5, 141.3, 140.2, 138.4, 132.7, 132.4, 132.1, 124.4, 121.6, 121.5, 118.7, 118.5, 117.9, 115.6, 115.3, 43.2; UV-vis (DMSO, nm) 340 (π–π*), 422 (*n*–π*); LC-MS *m/z* 794.0 [M − 1]

4.3.3 (*Z*)-2-(3-(2-(4,6-Bis(4-chlorophenoxy)-1,3,5-triazin-2-yl)hydrazineylidene)-2-oxoindolin-1-yl)-*N*-(4-bromophenyl)acetamide (7c). Yellow solid; melting point: 241–243 °C; R_f: 0.51 ($CHCl_3$, MeOH, 9 : 1); yield: 86%; FT-IR $\bar{\nu}$ (cm^{-1}): 1209 (C–N stretch; lactam), 1378 (C_{sp^2}–O stretch; ether), 1484, 1558 (C=C stretch; aromatic), 1619 (C=N stretch; imine), 1686, 1720 (C=O stretch; amide), 2981, (C_{sp^3}–H stretch), 3067, 3190 (C_{sp^2}–H stretch), 3225, 3300 (N–H stretch); ^{1}H NMR (300 MHz, DMSO-d_6) δ (ppm): 12.70 (s, 1H, –NH), 10.51 (s, 1H, –NH), 7.60–7.17 (m, 16H, Ar–H), 4.66 (s, 2H, $-CH_2$); ^{13}C NMR (75 MHz, DMSO-d_6) δ (ppm): 167.2, 165.3, 161.7, 150.6, 137.8, 135.8, 132.1, 130.5, 129.8, 129.2, 127.7, 124.0, 121.3, 119.4, 110.8, 43.2; UV-vis (DMSO, nm) 348 (π–π*); LC-MS *m/z* 704.2 [M − 1]

4.3.4 (*Z*)-2-(3-(2-(4,6-Bis(4-nitrophenoxy)-1,3,5-triazin-2-yl) hydrazineylidene)-2-oxoindolin-1-yl)-*N*-(4-bromophenyl)acetamide (7d). Yellow solid; melting point: 247–249 °C; R_f: 0.34 ($CHCl_3$, MeOH, 9 : 1); yield: 81%; FT-IR $\bar{\nu}$ (cm^{-1}): 1209 (C–N stretch; lactam), 1345 (C_{sp^3}–O stretch; ether), 1467 (C_{sp^3}–H bend; methylene), 1499, 1559 (C=C stretch; aromatic), 1619 (C=N stretch; imine), 1688 (C=O stretch; amide), 2872, (C_{sp^3}–H

stretch), 3070, 3124 (C_{sp^2}–H stretch), 3244, 3300 (N–H stretch); ^{1}H NMR (300 MHz, DMSO-d_6) δ (ppm): 12.78 (s, 1H, –NH), 10.51 (s, 1H, –NH), 8.34–7.17 (m, 16H, Ar–H), 4.67 (s, 2H, –CH_2); ^{13}C NMR (75 MHz, DMSO-d_6) δ (ppm): 167.3, 165.2, 145.5, 143.6, 138.3, 136.3, 132.1, 125.8, 123.4, 121.6, 119.6, 116.2, 43.2; UV-vis (DMSO, nm) 350 (π–π^*); LC-MS *m/z* 726.1 [M − 1]

4.3.5 (*Z*)-2-(3-(2-(4,6-Bis(*m*-tolyloxy)-1,3,5-triazin-2-yl)hydrazineylidene)-2-oxoindolin-1-yl)-*N*-(4-bromophenyl)acetamide (7e). Yellow solid; melting point: 237–238 °C; R_f: 0.57($CHCl_3$, MeOH, 9 : 1); yield: 83%; FT-IR $\bar{\nu}$ (cm^{-1}): 1202 (C–N stretch; lactam), 1366 (C_{sp^2}–O stretch; ether), 1467 (C_{sp^3}–H bend; methylene), 1487, 1541 (C=C stretch; aromatic), 1619 (C=N stretch; imine), 1684 (C=O stretch; amide), 2924 (C_{sp^3}–H stretch), 3049, 3129 (C_{sp^2}–H stretch), 3252, 3300 (N–H stretch); ^{1}H NMR (300 MHz, DMSO-d_6) δ (ppm): 12.52 (s, 1H, –NH), 10.52 (s, 1H, –NH), 7.83–6.57 (m, 16H, Ar–H), 4.68 (s, 2H, –CH_2); ^{13}C NMR (75 MHz, DMSO-d_6) δ (ppm): 166.0, 164.9, 156.7, 153.5, 150.4, 138.4, 132.1, 130.5, 129.8, 129.5, 124.0, 122.7, 121.6, 117.3, 43.2; UV-vis (DMSO, nm) 351 (π–π^*); LC-MS *m/z* 664.2 [M − 1]

4.3.6 (*Z*)-2-(3-(2-(4,6-bis(3-(Trifluoromethyl)phenoxy)-1,3,5-triazin-2-yl)hydrazineylidene)-2-oxoindolin-1-yl)-*N*-(4-bromophenyl)acetamide (7f). Yellow solid; melting point: 240–242 °C; R_f: 0.41 ($CHCl_3$, MeOH, 9 : 1); yield: 84%; FT-IR $\bar{\nu}$ (cm^{-1}): 1168 (C_{sp^3}–O stretch; ether), 1209 (C–N stretch; lactam), 1281 (C_{sp^2}–O stretch; ether), 1467 (C_{sp^3}–H bend; methylene), 1470, 1541 (C=C stretch; aromatic), 1619 (C=N stretch; imine), 1686 (C=O stretch; amide), 1737 (C=O stretch; ketone), 2971, (C_{sp^3}–H stretch), 3049, 3129 (C_{sp^2}–H stretch), 3225, 3300, (N–H stretch); ^{1}H NMR (300 MHz, DMSO-d_6) δ (ppm): 12.68 (s, 1H, –NH), 10.51 (s, 1H, –NH), 7.61–7.17 (m, 16H, Ar–H), 4.67 (s, 2H, –CH_2); ^{13}C NMR (75 MHz, DMSO-d_6) δ (ppm): 167.2, 165.3, 161.7, 158.4, 148.0, 143.5, 137.8, 135.7, 132.0, 129.2, 127.7, 123.9, 120.8, 119.4, 110.8, 43.2; UV-vis (DMSO, nm) 351 (π–π^*); LC-MS *m/z* 771.4 [M − 1]

Data availability

The additional data that support this manuscript is provided as part of ESI†

Conflicts of interest

The authors declare that there are no conflicts of interest

Acknowledgements

We are grateful to the Higher Education Commission (HEC) of Pakistan and The World Academy of Sciences (TWAS) for providing financial support through the projects (9225/Federal/NRPU/R&D/HEC/2017) and (13-419 RG/PHA/AS_CUNESCO FR: 3240279216), respectively.

References

1 B. Liu, H. Zhou, L. Tan, K. T. H. Siu and X.-Y. Guan, *Signal Transduction Targeted Ther.*, 2024, **9**, 175.
2 C. Zhao, W. Song, J. Wang, X. Tang and Z. Jiang, *Chem. Commun.*, 2025, **61**, 1962–1977.
3 N. K. Sharma, A. Bahot, G. Sekar, M. Bansode, K. Khunteta, P. V. Sonar, A. Hebale, V. Salokhe and B. K. Sinha, *Cancers*, 2024, **16**, 680.
4 S. Zheng, R. Chen, L. Zhang, L. Tan, L. Li, F. Long and T. Wang, *Eur. J. Med. Chem.*, 2024, 116702.
5 A. Mushtaq, P. Wu and M. M. Naseer, *Pharmacol. Ther.*, 2024, **254**, 108579.
6 D. Li, X. Peng, Z. Hu, S. Li, J. Chen and W. Pan, *Eur. J. Med. Chem.*, 2024, **264**, 115982.
7 A. Rismanbaf, *Cancer Rep.*, 2024, **7**, e1945.
8 A. M. Abu-Dief, T. El-Dabea, R. M. El-Khatib, M. Feizi-Dehnayebi, F. S. Aljohani, K. Al-Ghamdi, I. O. Barnawi and M. A. E. A. A. Ali, *J. Mol. Liq.*, 2024, **399**, 124422.
9 I. El-Deen, A. Shoair and M. El-Bindary, *J. Mol. Liq.*, 2018, **249**, 533–545.
10 G. Magdy, F. Belal, A. F. A. Hakiem and A. M. Abdel-Megied, *Int. J. Biol. Macromol.*, 2021, **182**, 1852–1862.
11 R. Wing, H. Drew, T. Takano, C. Broka, S. Tanaka, K. Itakura and R. E. Dickerson, *Nature*, 1980, **287**, 755–758.
12 L. Strekowski and B. Wilson, *Mutat. Res., Fundam. Mol. Mech. Mutagen.*, 2007, **623**, 3–13.
13 I. Saha, M. Hossain and G. Suresh Kumar, *J. Phys. Chem. B*, 2010, **114**, 15278–15287.
14 M. Sirajuddin, S. Ali and A. Badshah, *J. Photochem. Photobiol., B*, 2013, **124**, 1–19.
15 A. Ganguly, S. Ghosh and N. Guchhait, *Phys. Chem. Chem. Phys.*, 2015, **17**, 483–492.
16 J.-H. Shi, T.-T. Liu, M. Jiang, J. Chen and Q. Wang, *J. Photochem. Photobiol., B*, 2015, **147**, 47–55.
17 H. Li, X. Bu, J. Lu, C. Xu, X. Wang and X. Yang, *Spectrochim. Acta, Part A*, 2013, **107**, 227–234.
18 R. Bera, B. K. Sahoo, K. S. Ghosh and S. Dasgupta, *Int. J. Biol. Macromol.*, 2008, **42**, 14–21.
19 J.-H. Shi, J. Chen, J. Wang and Y.-Y. Zhu, *Spectrochim. Acta, Part A*, 2015, **136**, 443–450.
20 Y. Guo, Q. Yue and B. Gao, *Int. J. Biol. Macromol.*, 2011, **49**, 55–61.
21 N. Shakibapour, F. Dehghani Sani, S. Beigoli, H. Sadeghian and J. Chamani, *J. Biomol. Struct. Dyn.*, 2019, **37**, 359–371.
22 A. Mushtaq, U. Azam, S. Mehreen and M. M. Naseer, *Eur. J. Med. Chem.*, 2023, **249**, 115119.
23 M. Altamimi, S. A. Syed, B. Tuzun, M. R. Alhazani, O. Alnemer and A. Bari, *J. Enzyme Inhib. Med. Chem.*, 2024, **39**, 2288548.
24 N. S. Haiba, H. H. Khalil, M. A. Moniem, M. H. El-Wakil, A. A. Bekhit and S. N. Khattab, *Bioorg. Chem.*, 2019, **89**, 103013.
25 A. S. Diakité, C. N. t. M. Ambeu-Loko, A. D. Yapi, C. Logé, A. Kacou, S. Kra, B. Baratte, S. Bach, S. Ruchaud and D. Sissouma, *Int. J. Pharm. Res. Allied Sci.*, 2024, **13**, 1–11.
26 T. Verma, M. Sinha and N. Bansal, *Anti-Cancer Agents Med. Chem.*, 2020, **20**, 4–28.
27 I. Shawish, A. Barakat, A. Aldalbahi, A. M. Malebari, M. S. Nafie, A. A. Bekhit, A. Albohy, A. Khan, Z. Ul-Haq and M. Haukka, *ACS omega*, 2022, **7**, 24858–24870.

28 A. El-Faham, M. Farooq, Z. Almarhoon, R. Abd Alhameed, M. A. Wadaan, B. G. de la Torre and F. Albericio, *Bioorg. Chem.*, 2020, **94**, 103397.
29 Q. Dai, Q. Sun, X. Ouyang, J. Liu, L. Jin, A. Liu, B. He, T. Fan and Y. Jiang, *Molecules*, 2023, **28**, 4278.
30 K. Vine, L. Matesic, J. Locke, M. Ranson and D. Skropeta, *Anti-Cancer Agents Med. Chem.*, 2009, **9**, 397–414.
31 W. M. Eldehna, M. A. El Hassab, M. F. Abo-Ashour, T. Al-Warhi, M. M. Elaasser, N. A. Safwat, H. Suliman, M. F. Ahmed, S. T. Al-Rashood and H. A. Abdel-Aziz, *Bioorg. Chem.*, 2021, **110**, 104748.
32 D. A. Gideon, P. Annadurai, V. Nirusimhan, A. Parashar, J. James and V. V. Dhayabaran, in *Handbook of Oxidative Stress in Cancer: Therapeutic Aspects*, Springer, 2021, pp. 1–25.
33 K. Dhahagani, M. P. Kesavan, K. G. G. Vinoth, L. Ravi, G. Rajagopal and J. Rajesh, *Mater. Sci. Eng., C*, 2018, **90**, 119–130.
34 Y.-O. Teng, H.-Y. Zhao, J. Wang, H. Liu, M.-L. Gao, Y. Zhou, K.-L. Han, Z.-C. Fan, Y.-M. Zhang and H. Sun, *Eur. J. Med. Chem.*, 2016, **112**, 145–156.
35 V. R. Solomon, C. Hu and H. Lee, *Bioorg. Med. Chem.*, 2009, **17**, 7585–7592.
36 E. P. Başaran, S. Köprü, S. Akkoç and B. i. Türkmenoğlu, *ACS Omega*, 2024, **9**, 17551–17562.
37 R. Raju, K. Chidambaram, B. Chandrasekaran, M. F. Bayan, T. K. Maity, A. M. Alkahtani and H. C. Chandramoorthy, *J. Saudi Chem. Soc.*, 2023, **27**, 101598.
38 W. M. Eldehna, A. Altoukhy, H. Mahrous and H. A. Abdel-Aziz, *Eur. J. Med. Chem.*, 2015, **90**, 684–694.
39 M. M. El-Naggar, D. S. A. Haneen, A. B. M. Mehany and M. T. Khalil, *Int. J. Biol. Macromol.*, 2020, **150**, 1323–1330.
40 Y. Tamaddon-Abibigloo, S. Dastmalchi, N. Razzaghi-Asl and J. S. Mojarrad, *Bioorg. Chem.*, 2024, **147**, 107355.
41 H. H. Al-Rasheed, S. A. Al-Khamis, A. Barakat, A. A. Masoud, A. A. Sobhy, D. A. Ghareeb, B. G. de la Torre, F. Albericio and A. El-Faham, *Tetrahedron*, 2024, 134424.
42 A. Mushtaq and M. M. Naseer, *J. Mol. Struct.*, 2025, **1322**, 140558.
43 A. Mushtaq, R. Asif, W. A. Humayun and M. M. Naseer, *RSC Adv.*, 2024, **14**, 14051–14067.
44 T. Linder, M. Schnürch and M. D. Mihovilovic, *Monatsh. Chem.*, 2018, **149**, 1257–1284.
45 S. Federico, A. Ciancetta, N. Porta, S. Redenti, G. Pastorin, B. Cacciari, K. N. Klotz, S. Moro and G. Spalluto, *Eur. J. Med. Chem.*, 2016, **108**, 529–541.
46 Ö. Akgül, A. H. Tarikoğullari, F. A. Köse, P. B. Kirmizibayrak and M. V. Pabuççuoğlu, *Turk. J. Chem.*, 2013, **37**, 204–212.
47 L. Firoozpour, L. Gao, S. Moghimi, P. Pasalar, J. Davoodi, M.-W. Wang, Z. Rezaei, A. Dadgar, H. Yahyavi, M. Amanlou and A. Foroumadi, *J. Enzyme Inhib. Med. Chem.*, 2020, **35**, 1674–1684.
48 M. Mohanraj, G. Ayyannan, G. Raja and C. Jayabalakrishnan, *Mater. Sci. Eng., C*, 2016, **69**, 1297–1306.
49 J. Bai, Y. Li and G. Zhang, *Cancer Biol. Med.*, 2017, **14**, 348.
50 T. A. Farghaly, A. M. A. Alnaja, H. A. El-Ghamry and M. R. Shaaban, *Bioorg. Chem.*, 2020, **102**, 104103.
51 T.-R. Li, Z.-Y. Yang, B.-D. Wang and D.-D. Qin, *Eur. J. Med. Chem.*, 2008, **43**, 1688–1695.
52 H. Ullah, V. Previtali, H. B. Mihigo, B. Twamley, M. K. Rauf, F. Javed, A. Waseem, R. J. Baker and I. Rozas, *Eur. J. Med. Chem.*, 2019, **181**, 111544.
53 A. K. Das, S. I. Druzhinin, H. Ihmels, M. Müller and H. Schönherr, *Chem.–Eur. J.l*, 2019, **25**, 12703–12707.
54 H. Shinziya, R. S. Menon and A. K. Das, *RSC Adv.*, 2024, **14**, 30631–30646.
55 F. Arjmand and A. Jamsheera, *Spectrochim. Acta, Part A*, 2011, **78**, 45–51.
56 H. Ünver, B. Boyacıoğlu, C. T. Zeyrek, M. Yıldız, N. Demir, N. Yıldırım, O. Karaosmanoğlu, H. Sivas and A. Elmalı, *J. Mol. Struct.*, 2016, **1125**, 162–176.
57 S. Naz, S. Ullah, U. Iqbal, S. Yousuf, S. Rahim, N. Muhammad, R. Fatima, I. U. Haq, A. Haider and S. Ali, *J. Mol. Liq.*, 2022, **368**, 120792.
58 A. G. Ribeiro, S. M. V. de Almeida, J. F. de Oliveira, T. R. C. de Lima Souza, K. L. Dos Santos, A. P. de Barros Albuquerque, M. C. D. B. L. Nogueira, L. B. de Carvalho Junior, R. O. de Moura and A. C. da Silva, *Eur. J. Med. Chem.*, 2019, **182**, 111592.
59 A. K. Das, H. Ihmels and S. Kölsch, *Photochem. Photobiol. Sci.*, 2019, **18**, 1373–1381.
60 K. Jeyalakshmi, N. Selvakumaran, N. S. Bhuvanesh, A. Sreekanth and R. Karvembu, *RSC Adv.*, 2014, **4**, 17179–17195.
61 L. H. Abdel-Rahman, B. S. Al-Farhan, N. O. Al Zamil, M. A. Noamaan, H. E.-S. Ahmed and M. S. S. Adam, *Bioorg. Chem.*, 2021, **114**, 105106.
62 N. Yıldırım and N. Demir, *Sakarya Univ. J. Sci.*, 2021, **25**, 339–348.
63 T. Kondori, N. Akbarzadeh-T, H. Ghaznavi, Z. Karimi, R. Sheervalilou, M. Dušek, V. Eigner and O. Shahraki, *J. Mol. Struct.*, 2021, **1231**, 129989.
64 J.-H. Shi, D.-Q. Pan, K.-L. Zhou and Y.-Y. Lou, *J. Biomol. Struct. Dyn.*, 2019, **37**, 837–845.
65 L. Strekowski and B. Wilson, *Mutat. Res., Fundam. Mol. Mech. Mutagen.*, 2007, **623**, 3–13.
66 A. Granzhan, H. Ihmels and G. Viola, *J. Am. Chem. Soc.*, 2007, **129**, 1254–1267.
67 L. Subha, C. Balakrishnan, S. Thalamuthu and M. Neelakantan, *J. Coord. Chem.*, 2015, **68**, 1021–1039.
68 P. N. Craig, *J. Med. Chem.*, 1971, **14**, 680–684.
69 S. Vishnu, A. Nag and A. K. Das, *Anal. Methods*, 2024, **16**, 5263–5271.
70 K. Mahmood, Z. Akhter, F. Perveen, M. Bibi, H. Ismail, N. Tabassum, S. Yousuf, A. R. Ashraf and M. A. Qayyum, *RSC Adv.*, 2023, **13**, 11982–11999.
71 O. Trott and A. J. Olson, *J. Comput. Chem.*, 2010, **31**, 455–461.
72 S. K. Ramadan, H. S. Abd-Rabboh, A. A. A. Hafez and W. S. Abou-Elmagd, *RSC Adv.*, 2024, **14**, 16584–16599.
73 M. Miar, A. Shiroudi, K. Pourshamsian, A. R. Oliaey and F. Hatamjafari, *J. Chem. Res.*, 2021, **45**, 147–158.
74 K. K. Saini, R. K. Upadhyay, R. Kant, A. Vajpayee, K. Jain, A. Kumar, L. S. Kumar and R. Kumar, *RSC Adv.*, 2023, **13**, 27525–27534.

75 M. Raghu, C. P. Kumar, M. Prashanth, K. Y. Kumar, B. Prathibha, G. Kanthimathi, S. A. Alissa, H. A. Alghulikah and S. M. Osman, *New J. Chem.*, 2021, **45**, 13909–13924.
76 E. J. Lien, Z.-R. Guo, R.-L. Li and C.-T. Su, *J. Pharm. Sci.*, 1982, **71**, 641–655.
77 S. Jiang, Y. Jin, R. Yan and Z. Wang, *J. Mol. Struct.*, 2021, **1225**, 129295.
78 Z. Akbari, C. Stagno, N. Iraci, T. Efferth, E. A. Omer, A. Piperno, M. Montazerozohori, M. Feizi-Dehnayebi and N. Micale, *J. Mol. Struct.*, 2024, **1301**, 137400.
79 I. Ahmad, R. H. Pawara, R. T. Girase, A. Y. Pathan, V. R. Jagatap, N. Desai, Y. O. Ayipo, S. J. Surana and H. Patel, *ACS omega*, 2022, **7**, 21820–21844.
80 M. A. Mumit, T. K. Pal, M. A. Alam, M. A. Islam, S. Paul and M. C. Sheikh, *J. Mol. Struct.*, 2020, **1220**, 128715.
81 Y. A. Alghuwainem, H. M. Abd El-Lateef, M. M. Khalaf, A. A. Abdelhamid, A. Alfarsi, M. Gouda, M. Abdelbaset and A. Abdou, *J. Mol. Liq.*, 2023, **369**, 120936.
82 G. Bocci, E. Carosati, P. Vayer, A. Arrault, S. Lozano and G. Cruciani, *Sci. Rep.*, 2017, **7**, 6359.
83 A. Daina, O. Michielin and V. Zoete, *Sci. Rep.*, 2017, **7**, 42717.
84 D. E. Pires, T. L. Blundell and D. B. Ascher, *J. Med. Chem.*, 2015, **58**, 4066–4072.
85 V. P. DE, T. Blundell and D. Ascher, *PKCSM*, 2015, 5.
86 D. E. V. Pires, T. L. Blundell and D. B. Ascher, *J. Med. Chem.*, 2015, **58**, 4066–4072.
87 C. A. Lipinski, F. Lombardo, B. W. Dominy and P. J. Feeney, *Adv. Drug Delivery Rev.*, 1997, **23**, 3–25.
88 D. F. Veber, S. R. Johnson, H.-Y. Cheng, B. R. Smith, K. W. Ward and K. D. Kopple, *J. Med. Chem.*, 2002, **45**, 2615–2623.
89 M. S. Kumar, S. Pakrashy, S. Manna, S. M. Choudhury, B. Das, A. Ghosh, A. H. Seikh, M. Dolai and A. K. Das, *Anal. Methods*, 2025, **17**, 2125–2133.
90 C. Lambertucci, G. Marucci, D. Dal Ben, M. Buccioni, A. Spinaci, S. Kachler, K.-N. Klotz and R. Volpini, *Eur. J. Med. Chem.*, 2018, **151**, 199–213.
91 M. Caricato, M. J. Frisch, J. Hiscocks and M. J. Frisch, *Gaussian 09: IOps Reference*, Gaussian Wallingford, CT, USA, 2009.
92 *BIOVIA Discovery Studio Visualizer*, Dassault Systèmes Biovia, San Diego, CA, USA, 2016.
93 W. L. DeLano, *CCP4 Newsl. Protein Crystallogr*, 2002, **40**, 82–92.
94 R. A. Laskowski and M. B. Swindells, *J. Chem. Inf. Model.*, 2011, **51**, 2778–2786.
95 E. F. Pettersen, T. D. Goddard, C. C. Huang, G. S. Couch, D. M. Greenblatt, E. C. Meng and T. E. Ferrin, *J. Comput. Chem.*, 2004, **25**, 1605–1612.
96 K. Momma and F. Izumi, *J. Appl. Crystallogr.*, 2011, **44**, 1272–1276.